Altered Cl^- homeostasis hinders forebrain GABAergic interneuron migration in a mouse model of intellectual disability

Andrea Maset[a,b,c], Luisa Galla[c,d], Simona Francia[a,e], Olga Cozzolino[f,g], Paola Capasso[h], Rosa Chiara Goisis[c,d], Gabriele Losi[c,d], Angelo Lombardo[h,i], Gian Michele Ratto[f,g], and Claudia Lodovichi[a,b,c,d,1]

[a]Veneto Institute of Molecular Medicine, 35129 Padua, Italy; [b]Padova Neuroscience Center, 35129 Padova, Italy; [c]Department of Biomedical Sciences, University of Padua, 35131 Padua, Italy; [d]Neuroscience Institute, National Research Council, 35127 Padua, Italy; [e]Center for Synaptic Neuroscience and Technology, Istituto Italiano di Tecnologia, 16132 Genoa, Italy; [f]Istituto Nanoscienze, Consiglio Nazionale delle Ricerche, 56127 Pisa, Italy; [g]National Enterprise for nanoScience and nanoTechnology, Scuola Normale Superiore, 56127 Pisa, Italy; [h]San Raffaele Telethon Institute for Gene Therapy, IRCCS San Raffaele Scientific Institute, 20132 Milan, Italy; and [i]Vita-Salute San Raffaele University, 20132 Milan, Italy

Edited by Carol Ann Mason, Columbia University, New York, NY, and approved November 11, 2020 (received for review August 3, 2020)

Impairments of inhibitory circuits are at the basis of most, if not all, cognitive deficits. The impact of OPHN1, a gene associate with intellectual disability (ID), on inhibitory neurons remains elusive. We addressed this issue by analyzing the postnatal migration of inhibitory interneurons derived from the subventricular zone in a validated mouse model of ID ($OPHN1^{-/y}$ mice). We found that the speed and directionality of migrating neuroblasts were deeply perturbed in $OPHN1^{-/y}$ mice. The significant reduction in speed was due to altered chloride (Cl^-) homeostasis, while the overactivation of the OPHN1 downstream signaling pathway, RhoA kinase (ROCK), caused abnormalities in the directionality of the neuroblast progression in mutants. Blocking the cation–Cl^- cotransporter KCC2 almost completely rescued the migration speed while proper directionality was restored upon ROCK inhibition. Our data unveil a strong impact of OPHN1 on GABAergic inhibitory interneurons and identify putative targets for successful therapeutic approaches.

OPHN1 | intellectual disability | Cl homeostasis | 2P imaging | interneuron migration

Intellectual disability (ID) is a complex neurodevelopmental disorder characterized by a wide spectrum of social and cognitive dysfunctions, from mild alterations of cognition to distinctive symptoms of autism spectrum disorders (ASD). Among the most frequent ID genetic causes are single mutation on X-linked genes (XLID), such as FMR1, PCDH19, and Oligophrenin 1 (OPHN1). OPHN1 encodes for a Rho GTPase activating protein (Rho GAP) that is expressed in neuronal and glial cells, both during development and in adulthood, in brain areas with a high degree of plasticity such as the cortex, the hippocampus, and the olfactory bulb (OB) (1, 2). As a Rho GAP, OPHN1 modulates the activity of Rho GTPase proteins to orchestrate actin cytoskeleton remodeling, a process crucially involved in different steps of neuronal development (3). Several studies indicate that part of the ID pathology associated with OPHN1 mutation is a consequence of abnormal synaptic morphology and function linked to OPHN1 downstream enhanced RhoA kinase (ROCK) signaling and dysregulation of actin cytoskeleton dynamics (4–6). The mechanism underlying human ID associated with OPHN1 mutation, remains, however, unknown, suggesting that other mechanisms, not yet identified, contribute to the pathogenesis of ID.

Mounting evidence indicates that impairments of inhibitory circuits could be responsible for some clinical features of ID and could represent a unifying mechanism underlying the complexity of neurodevelopmental disorders, from ID to ASD (7–9). Concerning this aspect, the impact of OPHN1 mutation on GABAergic circuits remains elusive.

Most forebrain GABAergic inhibitory interneurons are born during embryonic life in the subpallial ganglionic eminence, from where they migrate tangentially to the cortical plate. A niche of neurogenesis persists in postnatal life along the wall of the lateral ventricles (subventricular zone, SVZ). From here, neuronal precursors migrate tangentially along the rostral migratory stream (RMS) to reach the OB, where they become mature interneurons. Additional ventral and dorsal routes, branching off the RMS, take the neuronal precursors to several cortical and subcortical areas in rodents (10) and also in human infants. Noteworthy, in human infants, the ventral pathway, indicated as the medial migratory stream, conveys new inhibitory interneurons to the prefrontal cortex, a region important for cognitive, social, and executive functions (11–13). The recruitment of these new inhibitory interneurons in the first postnatal months is thought to play a key role in postnatal brain plasticity, which is essential for normal brain development (12–15). Alterations of this process could therefore contribute to the pathogenesis of ID and ASD.

In previous work (16), we provided evidence that OPHN1 mutation impaired the morphology and synaptic functions of SVZ-derived inhibitory interneurons and caused a dramatic reduction in the number of precursors that reach the OB. Since the generation of neuronal precursors was not compromised in the SVZ of $OPHN1^{-/y}$ mice, we hypothesized that OPHN1 mutation could hinder the migration along the RMS, leading to the observed reduction of GABAergic neurons in the OB.

Significance

Intellectual disability associated with Oligophrenin 1 (OPHN1) mutation is a neurodevelopmental disorder characterized by a wide range of cognitive and social dysfunction. Here, we dissected the impact of OPHN1 mutation on the postnatal migration of inhibitory interneurons, a process that is thought to play a key role in postnatal developmental plasticity. We found that loss of function of OPHN1 led to an early maturation of the morphofunctional properties of the neuronal precursors that impaired their migration and resulted in a dramatically lower number of cells reaching their target area. We identified pharmacological treatments able to rescue the abnormal development of neuronal precursors and their migration.

Author contributions: C.L. designed research; A.M., L.G., S.F., O.C., R.C.G., G.L., G.M.R., and C.L. performed research; P.C. and A.L. contributed new reagents/analytic tools; A.M., S.F., O.C., G.L., G.M.R., and C.L. analyzed data; and C.L. wrote the paper.

The authors declare no competing interest.

This article is a PNAS Direct Submission.

[1]To whom correspondence may be addressed. Email: claudia.lodovichi@unipd.it.

This article contains supporting information online at https://www.pnas.org/lookup/suppl/doi:10.1073/pnas.2016034118/-/DCSupplemental.

Published December 29, 2020.

Here, by combining quantitative anatomy and two-photon time-lapse imaging, we found that the motility and the directionality of the neuronal precursor cells (NPC) were deeply perturbed in OPHN1$^{-/y}$ mice. In particular, we observed that GABA (γ-amminobutirric acid), a key regulator of NPC progression, elicited opposite effects on the motility of neuroblasts in OPHN1$^{-/y}$ mice with respect to controls. In line with postnatal development of intracellular chloride concentration ($[Cl^-]_i$) regulation in cortical neurons (17–19), we show that wild-type (WT) neuroblasts have a relatively high $[Cl^-]_i$, possibly supporting depolarizing GABA action. In contrast, mutant neuroblasts have an abnormally low $[Cl^-]_i$ due to the increased expression level of the Cl^- cotransporter KCC2 that in turn impairs NPC progression. Indeed, pharmacological inhibition of KCC2 almost completely restored the average speed of the migrating cells. This deregulation of Cl^- gradient due to premature expression of KCC2 stands as a novel element in the scenario of the causative role of Cl^- homeostasis in the etiopathogenesis of neurodevelopmental disorders (20–23). Noteworthy, the directionality of NPC migration was not affected by GABA signaling but was impaired by the OPHN1 downstream overactive ROCK. Indeed, inhibition of the overactive ROCK by fasudil, a clinically approved inhibitor of ROCK, completely rescued the directionality of NPC migration, without affecting their progression speed. Altogether our results demonstrate that OPHN1 mutation impairs the migration of postnatally generated inhibitory interneurons acting on two distinct signaling pathways that could provide new putative targets to design effective therapeutic strategies to restore proper migration of inhibitory interneurons.

Results

OPHN1 Mutation Disrupted the Chain Organization of Migrating Neuroblasts. The goal of this work is to study the impact of OPHN1 mutation on migrating neuroblasts. To this end, we first analyzed the architecture of the RMS in forebrain sagittal sections containing the SVZ and the OB. The stream of migrating cells was visualized by labeling neuronal precursors with antibodies against doublecortin (DCX), a marker of migrating cells. As reported in previous work (24–26), in controls the newly generated cells were organized in an orderly arrangement along the walls of the lateral ventricles and coalesced in chains to form the RMS and migrate to the OB (Fig. 1 *A*, *C*, *E*, and *G*). In OPHN1$^{-/y}$ mice, neuronal precursors exhibited a chaotic distribution of neuroblast chains that occupied significantly larger areas in the SVZ and in the OB in mutant than in control mice (Fig. 1 *B*, *D*, *F*, and *G*).

To investigate whether OPHN1 mutation affects the cellular organization of the RMS, sagittal sections of the brain containing the entire RMS, from the SVZ to the OB, were immunostained with antibodies against glial fibrillary acid protein (GFAP), a marker of astrocytes, and against DCX. High-magnification analysis of the forebrain confirmed that in controls neuroblasts travel tangentially in chains through tubular structures formed by specialized astrocytes. Processes of these astrocytes were oriented in parallel to the chains of migrating cells (Fig. 1 *H*, *J*, and *L*–*N*). In contrast, the arrangement of migrating cells was deeply disrupted in OPHN1$^{-/y}$ mice. Neuroblasts aggregated in shorter and thicker chains that broke significantly more often than in controls, constantly deviating from the tangential direction of migration (Fig. 1 *I*, *K*, and *L*–*N*). Furthermore, in mutant mice GFAP-positive astrocytic processes were chaotically intermingled with neuroblasts, often running across NPC chains (Fig. 1 *I* and *K*). The area occupied by astrocytic processes inside the RMS in OPHN1$^{-/y}$ mice was more than twice as large as in controls (Fig. 1*O*).

Then, we studied the distribution of the newly generated cells along the tangential axis of the RMS in controls and OPHN1$^{-/y}$ mice injected with 5-bromo-2′-deoxyuridine (BrdU), a marker of cell division. These mice were analyzed 7 d postinjection (dpi). As shown in Fig. 2, in controls almost no neuroblasts could be detected in the most caudal portion of the RMS (indicated as RMS1), as most cells had already reached the central part of the RMS (RMS2) and the OB (Fig. 2 *A*, *C*, *E*, and *G*). A completely different spatial distribution was observed in OPHN1$^{-/y}$ mice, where the vast majority of the newly generated cells clumped in the caudal portion of the RMS (RMS1) and only very few neuroblasts reached RMS2 and the OB (Fig. 2 *B*, *D*, *F*, and *G*).

Mutation of OPHN1 Impaired Neuroblast Morphology and Directionality. Most migrating neuroblasts have a "unipolar" morphology, characterized by a round-oblong soma and a long leading process that determines the directionality of migration (Fig. 2*H*). As a consequence of the strict link between structure and function of the leading process (27–30), alterations in NPC morphology could deeply affect their progression along the RMS. To further investigate the cellular consequence of the null mutation of OPHN1 on migrating cells, we analyzed the morphology of precursors. Lentiviral vectors expressing green fluorescent protein (GFP) were injected in the SVZ to label the newly generated cells and their morphology was analyzed 7 dpi, in sagittal sections of the brain. To visualize the entire RMS, these sections were immunostained with an antibody against DCX. From the SVZ to the core of the OB, the vast majority of control migrating neuroblasts exhibited a small oblong soma with a single leading process. A small percentage of cells presented two leading processes (indicated as bipolar cells) and only a few had multiple leading processes (Fig. 2*H*). The latter were located mostly in the central portion of the RMS and in the core of the OB (Fig. 2*I*). In contrast, in OPHN1$^{-/y}$ mice, there was a significant decrease in monopolar cells and a significant increase in bipolar and multipolar cells along the entire RMS and in the core of the OB (Fig. 2 *H* and *I*).

Altered Progression of Neuroblasts along the RMS in OPHN1$^{-/y}$. We reasoned that to study a dynamic phenomenon, such as migration, we needed to visualize the ongoing process. To this end, lentiviral vectors expressing GFP were injected in the SVZ to label newly generated cells. Four to five days after the viral injection, neuroblast migration was recorded in thick sagittal sections of the brain, containing the entire RMS (from the SVZ to the OB), by means of two-photon imaging.

The GFP-labeled cell population exhibited the typical morphology of migrating neuroblasts: an oblong soma and a leading process (Fig. 3 *A*–*F* and Movie S1). Neuroblasts progress along the RMS by the sequential elongation and retraction of the leading process (29, 30) and migrate in a saltatory manner, alternating phases of stop and go (Movie S2) (28, 30, 31). Due to the saltatory nature of neuroblast motility, quantitative assessment of neuroblast migration was computed with distinct parameters: 1) The average speed (micrometers per hour) indicates the rate of migration of a given neuroblast, including the time when it pauses, 2) the instantaneous speed (micrometers per minute) indicates the rate of migration when a given neuroblast is moving, excluding the pausing phases, and 3) the percentage of moving time reports the fraction of time in which a cell is moving during the time-lapse recording. It should be noted that most studies of time-lapse imaging of neuroblast migration reported only the average speed as defined by the distance traveled over a given period (32–34). This measurement is ambiguous since it cannot discriminate whether changes in average speed are due to changes in instantaneous speed or differences in the duration of pauses. By computing average speed and percentage of moving time we can identify which parameter is specifically affected and unveil differences that could not be appreciated otherwise. It is known that neuroblast progression toward the bulb is discontinuous not only in time, that is, saltatory, as indicated above, but also in space (32, 35). Along the RMS, precursors move both toward and afar from the OB, although the net migration is toward the OB. To ascertain whether the directionality of the migrating cells

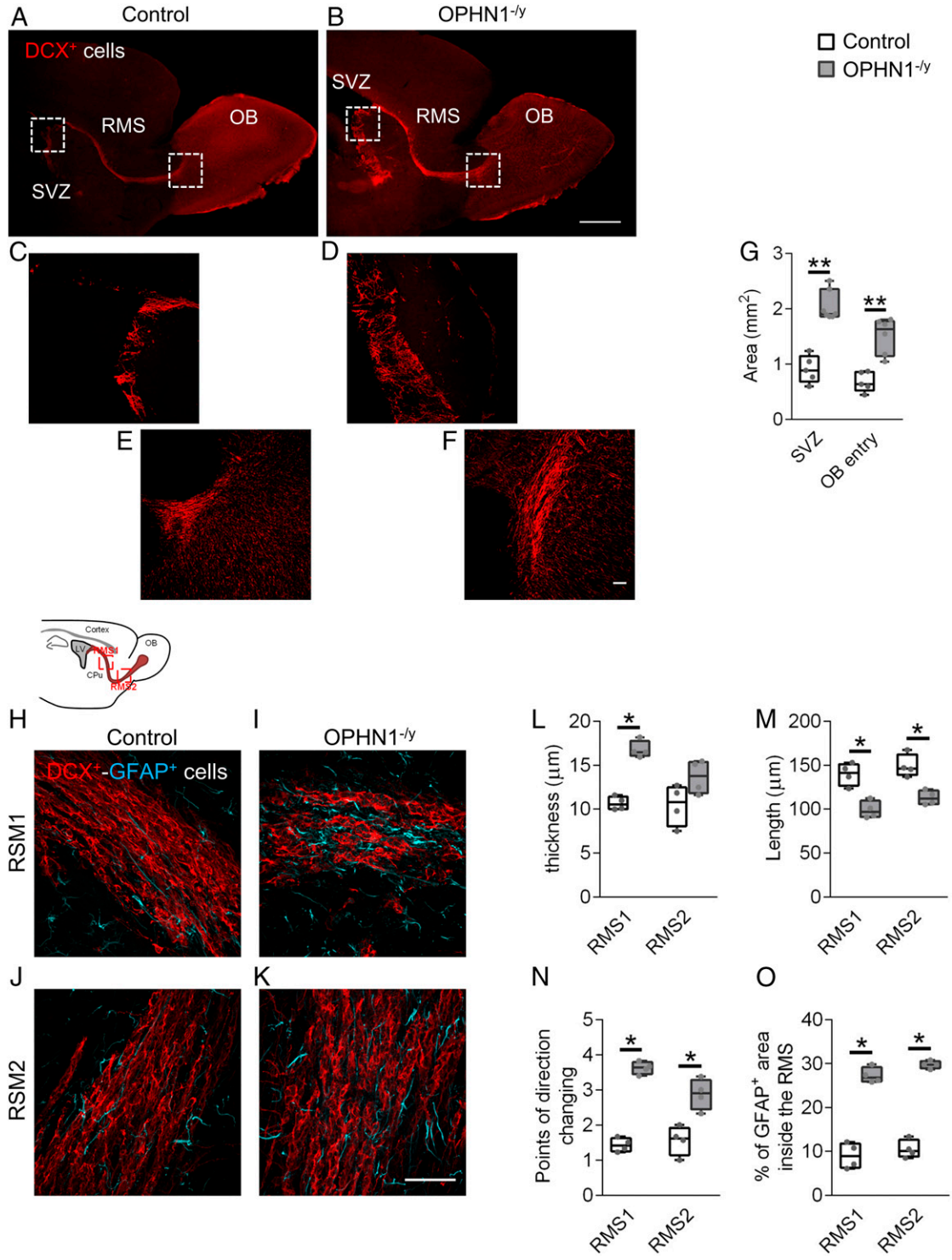

Fig. 1. Spatial organization of neuronal precursors along the RMS is altered in OPHN1$^{-/y}$ mice. (*A* and *B*) Low-magnification images of sagittal forebrain sections containing the SVZ, the RMS, and the OB. Migrating neuroblasts along the RMS are labeled with DCX (in red) in WT mice (*A*) and in OPHN1$^{-/y}$ mice (*B*). In OPHN1$^{-/y}$ mice the spatial distribution of the neuroblasts along the RMS is disrupted with respect to littermate controls. (*C*–*F*) High magnification of the regions highlighted in the dotted squares: the SVZ in WT mice (*C*) and OPHN1$^{-/y}$ mice (*D*) and the entry of the RMS into the OB in WT mice (*E*) and OPHN1$^{-/y}$ mice (*F*). The orderly arrangement of chains (*Left*) is deeply subverted in OPHN1$^{-/y}$ mice (*Right*). (Scale bars: *A* and *B*, 1 mm; *C*–*F*, 100 μm.) (*G*) Quantification of the areas highlighted in *C*–*F* in OPHN1$^{-/y}$ mice and WT mice. Bars = minimum to maximum. *P* values: 0.001 < ** < 0.01. (*H*–*K*) High-magnification images of the caudal (RMS1; *H*, *I*) and central (RMS2; *J*, *K*) portion of the RMS in control and OPHN1$^{-/y}$ mice. Migrating neuroblasts are labeled with DCX (in red), astrocytic processes are labeled with GFAP (in cyan). (Scale bar: 50 μm.) In controls, astrocytic processes run parallel to the orderly distributed chains of migrating cells, while in OPHN1$^{-/y}$ mice they appear thicker and invade untidy chains of migrating neuroblasts. (*L*–*O*) Quantification of the geometrical arrangement of neuroblasts' chains along the RMS in control mice and in OPHN1$^{-/y}$ mice in the two regions of interest. (*L*) Chains' thickness in RMS1 and in RMS2. (*M*) Chains' length in RMS1 and in RMS2. (*N*) Number of breaking points in RMS1 and in RMS2. (*O*) Areas occupied by astrocytic processes in RMS1 and in RMS2. Bars = minimum to maximum. *P* values: 0.01 < * < 0.05.

could be impaired in OPHN1$^{-/y}$ mice, we computed the percentage of cells moving toward the OB. Time-lapse imaging was performed for 2 h per condition, to ensure that both the migrating and stationary phases of neuroblasts were recorded. Recording for less than 1 h risks underestimating the average speed, because the active migration is present only for a limited amount of time (about 38 to 40%, discussed below) with respect to the total imaging time. Altogether, this approach allowed us to track and quantify the key aspects of neuroblast motility.

We first analyzed neuroblast migration along the RMS in basal conditions in control (Movie S3) and OPHN1$^{-/y}$ (Movie S4) mice. In controls, neuronal precursors migrated at an average speed of 42.8 ± 3.2 μm/h, with an instantaneous speed of 1.8 ± 0.4 μm/min. The percentage of time spent in active migration (moving time) was 38.2 ± 1.8%. Although the majority (77.6 ± 0.1%) of the migrating cells move toward the OB, that is, caudo-rostral progression along the RMS, we observed a few cells moving in the opposite direction that is, rostro-caudal, and also along the mediolateral directions, as reported previously (32, 35) (Fig. 3 *A*, *C*, *E*, and *G*–*J*). Time-lapse sequences recorded in OPHN1$^{-/y}$ mice offer a completely different scenario. Cells spent most of the time pausing, as confirmed by the significantly reduced percentage of moving time (28.8 ± 1.4%). Noteworthy, pausing neuroblasts extended and retracted several processes in different directions as if they were testing the environment to find a way to progress (Movie S5). This abnormal behavior hindered the progression of the neuroblasts since they moved for a reduced amount of time (see above and Fig. 3 statistics in *SI Appendix*) at a lower speed, (average speed, 24.7 ± 0.9 μm/h, instantaneous speed 1.4 ± 0.03 μm/min). Furthermore, only 53.1 ± 5.6% of the cells were observed moving toward the OB in OPHN1$^{-/y}$ mice in contrast to the ~ 80% of cells migrating to the OB in controls (Fig. 3 *B*, *D*, *F*, and *G*–*J*). Altogether these data indicate that the motility and the directionality of neuroblasts were deeply perturbed in OPHN1$^{-/y}$ mice (Fig. 3).

Abnormal Response to GABA in OPHN1$^{-/y}$ Migrating Cells. GABA is well known to modulate neuroblast motility along the RMS. GABA, abundantly available in the RMS, is produced by neuronal precursors, on which it acts via $GABA_A$ receptor ($GABA_AR$) (32, 36), in a paracrine and autocrine manner (32, 37). The level of ambient GABA in the RMS is thought to be maintained through a balance between GABA secretion by neuroblasts and GABA uptake performed by specialized astrocytes.

We observed, in agreement with previous work (32), that, upon GABA (10 μM) application, the average speed was significantly reduced as a consequence of the reduction of the percentage of time that neuroblasts spent in active migration. The moving speed (i.e., the instantaneous speed) remained, however, unaffected by GABA treatment (Fig. 4 *A*–*D*). Application of bicuculline, a blocker of $GABA_AR$, triggered a faster progression of migrating cells by increasing the percentage of active migration, which resulted in higher average speed, with no effect on the instantaneous speed (Fig. 4 *F*–*I*).

Surprisingly, GABA application had the opposite effect on OPHN1$^{-/y}$ neuroblasts. It caused a significant increase in the average speed, primarily because migrating cells moved faster. However, since the percentage of moving time in OPHN1$^{-/y}$ mice was not affected, the average speed was lower than in controls (Fig. 4 *A*–*D*). Bicuculline reduced the average speed, acting both on the percentage of moving time and on the moving speed of OPHN1$^{-/y}$ neuroblasts (Fig. 4 *F*–*I*). These results indicated that GABA acts on migrating cells via $GABA_ARs$ in both conditions, but it elicits opposite effects in control and mutant mice. Neither in controls nor in OPHN1$^{-/y}$ mice did GABA, and the antagonist of $GABA_ARs$, bicuculline, influence the directionality of migrating cells (Fig. 4 *E* and *J*).

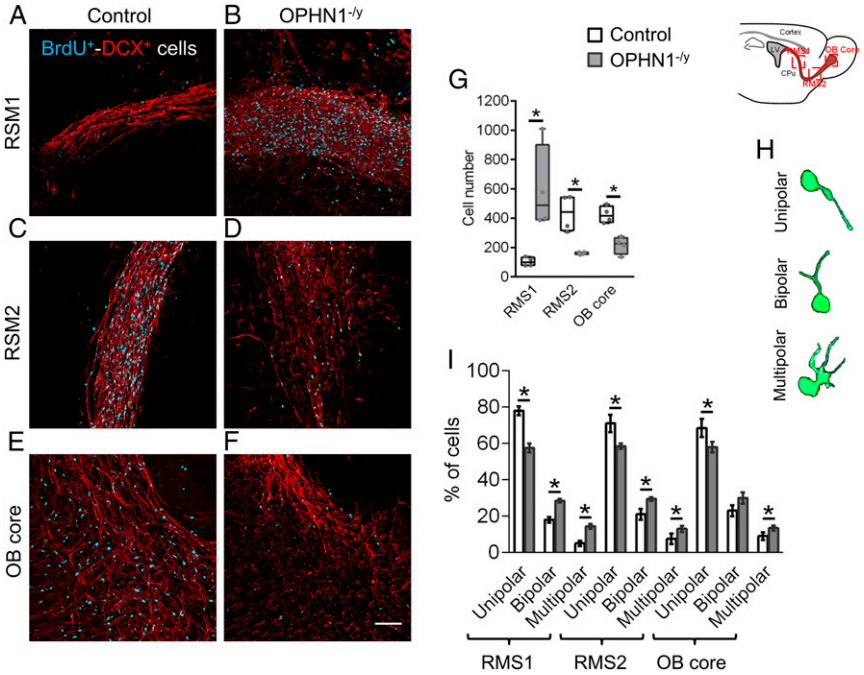

Fig. 2. Neuronal precursors distribution and morphology are perturbed in OPHN1$^{-/y}$ mice. (*A*–*F*) Distinct distribution of the complement of newly generated cells, stained with BrdU (in cyan) along the stream of migrating labeled with DCX (in red) in control mice (*A*, *C*, and *E*) and OPHN1$^{-/y}$ mice (*B*, *D*, and *F*) (Scale bar: 200 μm.) (*G*) Quantitative analysis of neuronal precursors distribution in control and in OPHN1$^{-/y}$ mice in RMS1, in RMS2 and in the core of the OB. Bars = minimum to maximum. *P* values: 0.01 < * < 0.05. (*H* and *I*) Morphological types of migrating neuroblasts. Examples of different neuroblast types in which the green fluorescence was enhanced to saturation, offline (*H*), and their quantification (*I*) along the RMS at 7 dpi in control mice and OPHN1$^{-/y}$ mice in RMS1, RMS2, and in the core of the OB. Bars = SEM. *P* values: 0.01 < * < 0.05.

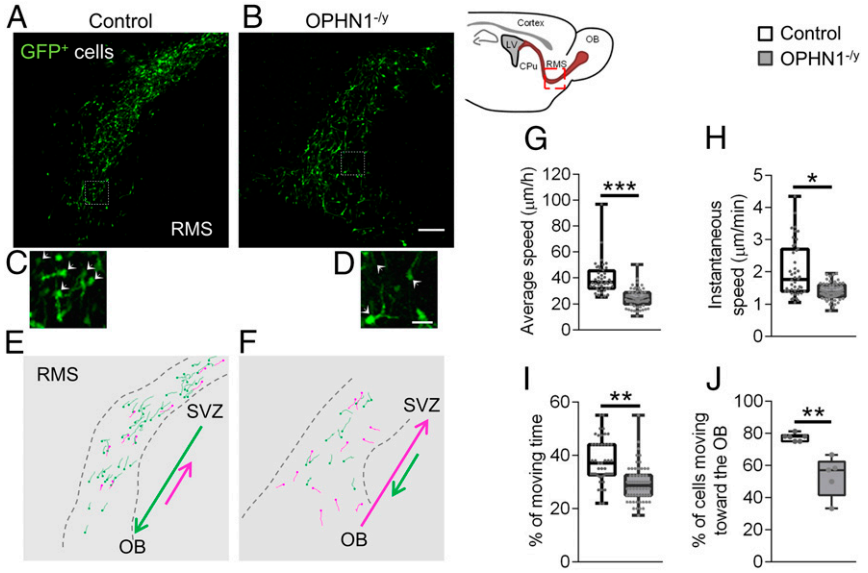

Fig. 3. Migration of neuronal precursors along the RMS is deeply hampered in OPHN1$^{-/y}$ mice. (*A* and *B*) Stop frames of time-lapse imaging of GFP-labeled neuroblasts in sagittal forebrain sections in control (*A*) and OPHN1$^{-/y}$ mice (*B*). (Scale bar: 100 µm.) (*C* and *D*) High magnification of the areas in the dotted squares in *A* and *B*, respectively. Neuroblasts, indicated by arrows, migrate toward the OB (*C*) and away from the OB (*D*). The direction of migration is dictated by the orientation of the leading processes. (Scale bar: 10 µm.) (*E* and *F*) Drawings of the cells in *A* and *B*, respectively. In green: cells migrating toward the OB; in magenta: cells migrating away from the OB. (*G–J*) Quantitative analysis of the migration along the RMS in control mice and in OPHN1$^{-/y}$ mice. (*G*) Average migration speed. (*H*) Instantaneous speed. (*I*) Percentage of moving time. (*J*) Directionality of migration. Bars = minimum to maximum. *P* values: 0.01 < * < 0.05; 0.001 < ** < 0.01; *** < 0.001.

Altered Cl$^-$ Homeostasis in OPHN1$^{-/y}$ Migrating Cells. The different responses elicited by GABA in control and OPHN1$^{-/y}$ NPC suggest that the activation of $GABA_A$ Rs has different outcomes in control and mutant mice. The current flowing through the $GABA_A$ R is given by

$$I_{GABA} = g_{GABA}(V_m - E_{Cl}) \qquad E_{Cl} = \frac{RT}{zF} ln\left(\frac{[Cl^-]_i}{[Cl^-]_o}\right),$$

where g_{GABA} is the conductance, V_m is the membrane potential, and E_{Cl} indicates the reversal potential for Cl. Therefore, the direction of the current flowing through the $GABA_AR$ depends on both $[Cl^-]_i$ and membrane potential and both factors should be considered.

First, we measured $[Cl^-]_i$ in migrating precursors by means of two-photon imaging based on the genetically encoded Cl$^-$ sensor LssClopHensor (17). The plasmid coding for the sensor was electroporated in the SVZ and $[Cl^-]_i$ was measured in individual migrating cells imaged in acute slices, 5 to 6 d after the electroporation (Fig. 5*A*). We observed that, in control mice, neuronal precursors are characterized by high $[Cl^-]_i$ (33.8 ± 18.9 mM) corresponding to an estimated E_{Cl}^- of −36 ± 16 mV. These NPC features recapitulate the profile of immature cortical neurons in early postnatal development (35, 36). In contrast, in OPHN1$^{-/y}$ mice $[Cl^-]_i$ was significantly reduced (16.6 ± 9.2 mM), with correspondingly lower values of E_{Cl}^- (−57 ± 20 mV) (Fig. 5 *A–C*), thus resembling the values observed in mature cortical neurons.

We then evaluated the second factor that regulates the direction of ion current through $GABA_A$Rs, that is, V_m, and to this end we directly measured the reversal potential of $GABA_A$R-mediated Cl$^-$ currents by performing gramicidin-perforated patch-clamp recordings. To label NPC, lentiviruses expressing mKate were injected in the SVZ of control and OPHN1$^{-/y}$ mice (see *SI Appendix*, *Supplementary Methods* for details). Brain slices were prepared from WT control and OPHN1$^{-/y}$ mice and migrating neuroblasts were identified by the expression of mKate and by their localization in the RMS. We locally applied muscimol, a selective $GABA_AR$ agonist, at different holding potentials to evaluate E_{Cl}^- (Fig. 5 *D* and *E*). As shown by Fig. 5 *D* and *E*, $GABA_AR$-mediated Cl$^-$ currents measured in OPHN1$^{-/y}$ mice have significantly more negative E_{Cl}^- values than in WT mice (E_{Cl}^- = −51.1 ± 7.2 mV and −26.3 ± 4.5 mV for OPHN1$^{-/y}$ and WT, respectively). Consistently with the imaging data, the electrophysiological measurements of E_{Cl}^- confirmed that RMS neuroblasts of OPHN1$^{-/y}$ mice have significantly lower $[Cl^-]_i$ than WT mice, ($[Cl^-]_i$ = 23.5 ± 6.8 mM and 50 ± 7.0 mM for OPHN1$^{-/y}$ and WT, respectively) (Fig. 5*E*). It is noteworthy that we found that neuroblasts resting membrane potentials, indicated as V_{rest}, was similar in WT and in OPHN1$^{-/y}$ mice (V_{rest} WT = −62.2 ± 12.2 mV and V_{rest} OPHN1$^{-/y}$ = −58.9 ± 10.2 mV, respectively; *SI Appendix*, Fig. S1). Altogether, these data show that in a large portion of OPHN1$^{-/y}$ neuroblasts GABA response was hyperpolarizing (44% of cells tested) while in WT mice this type of response occurred only in one out of eight cells tested (equivalent to 12.5%).

$[Cl^-]_i$ is regulated by the opposite actions of two cotransporters: the Na-K-2Cl cotransporter, NKCC1, and the K-Cl cotransporter, KCC2 (18, 38). NKCC1 is largely expressed in immature cells, including migrating neuroblasts along the RMS (33), and favors high $[Cl^-]_i$, leading to depolarization in response to GABA. KCC2 favors low $[Cl^-]_i$, promoting hyperpolarizing GABA responses. To investigate whether the opposite effects elicited by GABA in control and OPHN1$^{-/y}$ migrating cells could be ascribed to altered $[Cl^-]_i$ regulation, time-lapse imaging of migrating cells was performed in presence of bumetanide, an inhibitor of NKCC1, that is largely expressed in migrating cells along the RMS (30). In presence of bumetanide, control neuroblasts moved at lower speed and for a shorter amount of time in respect to basal conditions (Fig. 6 *A–D*). Bumetanide, however, did not affect mutant NPC progression, except for the increase of the instantaneous speed of migrating cells in OPHN1$^{-/y}$ mice (Fig. 6 *A–D*). On the contrary, the blocker of KCC2, VU0463271, did not exert any effect in controls but completely rescued the instantaneous speed and significantly increased the average speed and the percentage of moving

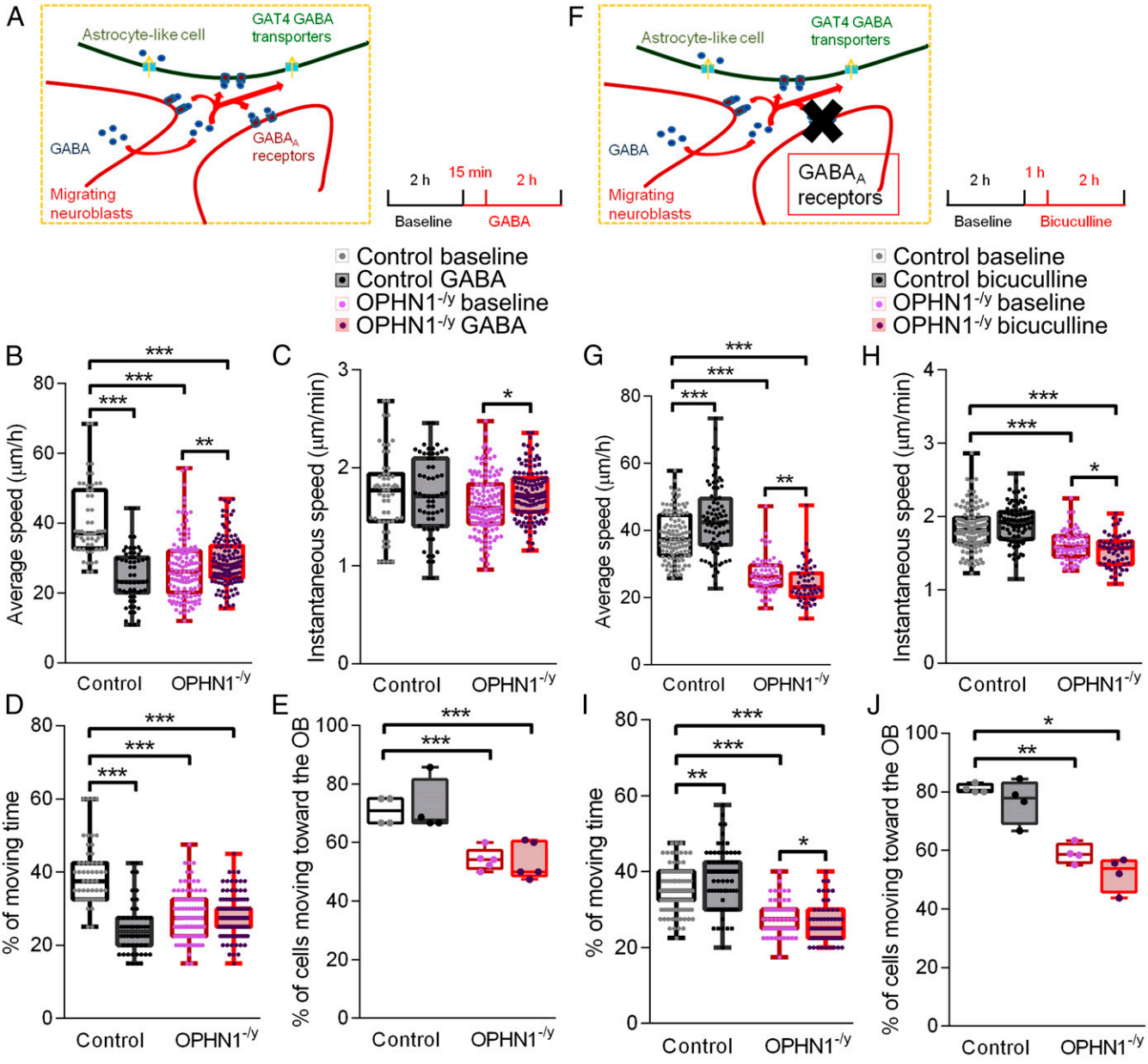

Fig. 4. GABA elicits opposite effects on the motility of neuronal precursors in control and OPHN1$^{-/y}$ mice. (*A* and *F*) Schematic of the source and targets of GABA along the RMS. GABA is produced by neuronal precursors (outlined in dark red) on which it acts, via GABA$_A$ receptors, in a paracrine and autocrine manner. The level of ambient GABA in the RMS is thought to be maintained through a balance between GABA secretion by neuroblasts and GABA uptake, by specialized astrocytes (outlined in dark green). The insets show the timing of drug delivery to the slices during time-lapse imaging. (*B–E*) Effects of acute GABA application on slices during time-lapse imaging of migrating neuroblasts in WT mice (black boxes) and in OPHN1$^{-/y}$ mice (red boxes). (*B*) GABA reduces the average speed of neuroblasts in WT mice, while increases neuroblast motility in OPHN1$^{-/y}$ mice. (*C*) GABA increases instantaneous speed in OPHN1$^{-/y}$ mice but not in WT mice, whereas (*D*) it reduces the percentage of moving time only in controls. (*E*) Directionality of migration is not affected by GABA. (*G–J*) Impact of the GABA competitive antagonist, bicuculline, on migrating cells in WT mice (black boxes) and in OPHN1$^{-/y}$ mice (red boxes). (*G*) Acute bicuculline application increases average migration speed in controls, while it reduces the average speed in OPHN1$^{-/y}$ mice. (*H*) Bicuculline decreases instantaneous speed in OPHN1$^{-/y}$ mice, with no effect on WT mice, whereas (*I*) it lowers the percentage of moving time in control and in mutant mice. (*J*) Directionality of migration is not affected by bicuculline. Bars = minimum to maximum. *P* values: 0.01 < * < 0.05; 0.001 < ** < 0.01; *** < 0.001.

time, which reached almost control levels, in OPHN1$^{-/y}$ mice (Fig. 6 *F–I*).

The directionality of neuronal precursors along the RMS again remained unaffected (discussed above) in control and in mutant mice treated with the inhibitors of NKCC1 or KCC2 (Fig. 6 *E* and *J*), suggesting that this feature is regulated by a different mechanism than GABA signaling.

The lower $[Cl^-]_i$ in OPHN1 mutants could be ascribed to altered expression of the Cl^- cotransporters. By analyzing NKCC1 and KCC2 protein expression along the RMS we found that the expression of KCC2 was significantly increased in OPHN1$^{-/y}$ mice with respect to controls, while the expression of NKCC1 was unaffected (*SI Appendix*, Fig. S2).

The Inhibitor of the ROCK, Fasudil, Rescued the Directionality of Migrating Cells in OPHN1$^{-/y}$ Mice. The loss of function of OPHN1 leads to overactivation of the ROCK downstream pathway (16, 39–41). Fasudil, a ROCK inhibitor, was shown to rescue some of

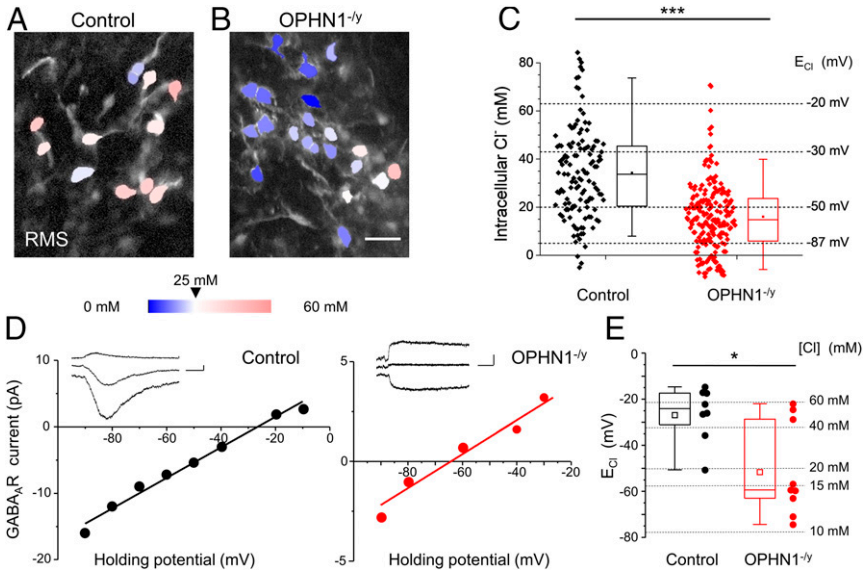

Fig. 5. Low intracellular chloride concentration ($[Cl^-]_i$) in neuroblasts in OPHN1$^{-/y}$ mice. (*A* and *B*) Representative pseudocolor two-photon images of LssClopHensor-labeled migrating neuroblasts along the RMS, in control mice (*A*) and OPHN1$^{-/y}$ mice (*B*), at 910-nm laser wavelength, and the relative lookup table. Cells with lower $[Cl^-]_i$ in blue, cells with higher $[Cl^-]_i$ in light red. (Scale bar: 200 μm.) (*C*) $[Cl^-]_i$ values (left *y* axis) and calculated E_{Cl}^- (right *y* axis) in neuronal precursors along the RMS in WT mice (black box) and in OPHN1$^{-/y}$ mice (red box). Bars = SD. *P* value: *** < 0.001. The intracellular chloride concentration is significantly lower in neuronal precursors in OPHN1$^{-/y}$ mice with respect to littermate controls. (*D*) Examples of current–voltage relationships of $GABA_A$-mediated currents recorded in RMS neuroblasts by gramicidin-perforated patch-clamp experiments in slices from WT (*D*, *Left*) and OPHN1$^{-/y}$ (*D*, *Right*) mice. Chloride reversal potential (E_{Cl}^-) value is measured as *x*-axis intercept of linear fit. Insets show sample traces of muscimol induced $GABA_AR$ mediated currents at −90, −60, and −10 mV for WT and −90, −60, and −30 mV for OPHN1$^{-/y}$. (Scale bars: 1 s, 2 pA.) (*E*) E_{Cl}^- values (left *y* axis) and calculated Cl^- intracellular concentrations ($[Cl^-]_i$) (right *y* axis) for WT and OPHN1$^{-/y}$ mice. Migrating neuroblasts in OPHN1$^{-/y}$ mice show lower E_{Cl}^- that in WT mice. Bars = minimum to maximum. *P* value: 0.01 < * < 0.05.

the cellular alterations triggered by OPHN1 mutation (16, 39, 42, 43), including the number of precursors that reach the OB at 15 dpi in OPHN1$^{-/y}$ mice (16). To decipher the effects of ROCK inhibition on migration, we performed time-lapse imaging of migrating cells in presence of fasudil. We found that neither the speed nor the percentage of moving time was affected by acute fasudil treatment in control and in OPHN1$^{-/y}$ mice (Fig. 7 *A*–*D*). Remarkably, fasudil rescued the directionality of migrating cells in OPHN1$^{-/y}$ mice while it did not exert any effect in controls (Fig. 7 *A* and *E*). These results suggest that upon fasudil treatment mutant neuroblasts would reach the OB with a certain delay in respect to controls. To corroborate this hypothesis, OPHN1$^{-/y}$ mice were chronically treated with fasudil for 3 wk and the number of newly generated cells that reaches the OB was quantified 9 d after BrdU injections. It is known that by this time point the whole complement of newly generated cells has already reached the OB (44), since the number of new cells that arrive in the OB is similar at 9 and 15 dpi (16).

Here, we found that at 9 dpi the complement of cells located in RMS2 was similar in WT and OPHN1$^{-/y}$ mice treated with fasudil (*SI Appendix*, Fig. S3). However, the number of cells that reached the core of the OB was still significantly lower in mutants treated with fasudil than in WT, although significantly higher than in nontreated OPHN1$^{-/y}$ mice, (*SI Appendix*, Fig. S3 and Fig. 7 *F*–*H*). As Redolfi et al. (16) found that fasudil treatment rescued the whole complement of newly generated cells that arrive in the OB at 15 dpi, the present data confirm that fasudil rescues the directionality, not the speed, of mutant forebrain GABAergic neuroblasts. Furthermore, we found that in mutant neuroblasts chronically treated with fasudil the expression of KCC2 remained significantly higher while the expression of NKCC1 was unperturbed with respect to controls (*SI Appendix*, Fig. S4). These results indicate that fasudil does not affect Cl^- cotransporters expression.

Discussion

Here, we demonstrate that ID-associated OPHN1 mutation deeply impairs the migration of forebrain GABAergic interneurons, generated postnatally in the SVZ.

We found that, in OPHN1$^{-/y}$ mice, the architecture of the RMS was deeply disrupted, with shorter and thicker NPC chains that break significantly more often than in controls. Time-lapse imaging showed that the aberrant chain architecture reflected the slower progression of mutant NPC. This slow migration was mostly due to a reduction in the amount of the time spent in active migration, and to a lesser extent to a lower moving speed. As a result of this hindered migration, neuroblasts accumulated in the most caudal portion of the RMS.

Migration is a dynamic process regulated by the highly tuned coordination of cell-autonomous and extrinsic factors. At the cellular level, the impaired migration associated with OPHN1 mutation could be ascribed to enhanced RhoA signaling and the consequent deregulation of actin cytoskeleton dynamics, which is a crucial determinant of cell morphology and regulates progression and directionality of migration (45–47). Migrating neuroblasts exhibit a small soma and a single leading process, which is critical for the motility and the directionality of the precursors. Indeed, the saltatory movement of NPC involves the extension, swelling formation, and retraction of the leading process that trail the soma and push forward the cells. Each of these steps is finely regulated by Rho GTPases and their regulators, Rho GEF (guanine nucleotide exchange factors) and Rho GAP. Specifically, Rac1 and Vac3 (GEF) were reported to be required during the extension of the leading process (48, 49), controlling the accumulation of F-actin. RhoA signaling, activated during the swelling formation (50), mediates soma movement (29, 51). Furthermore, the imbalance between the activity of Rac1 (and to a lesser extent Cdc42) and RhoA is likely to lead to the formation of overabundant leading processes (29, 49, 51). Mutation in the Rho GAP OPHN1 could

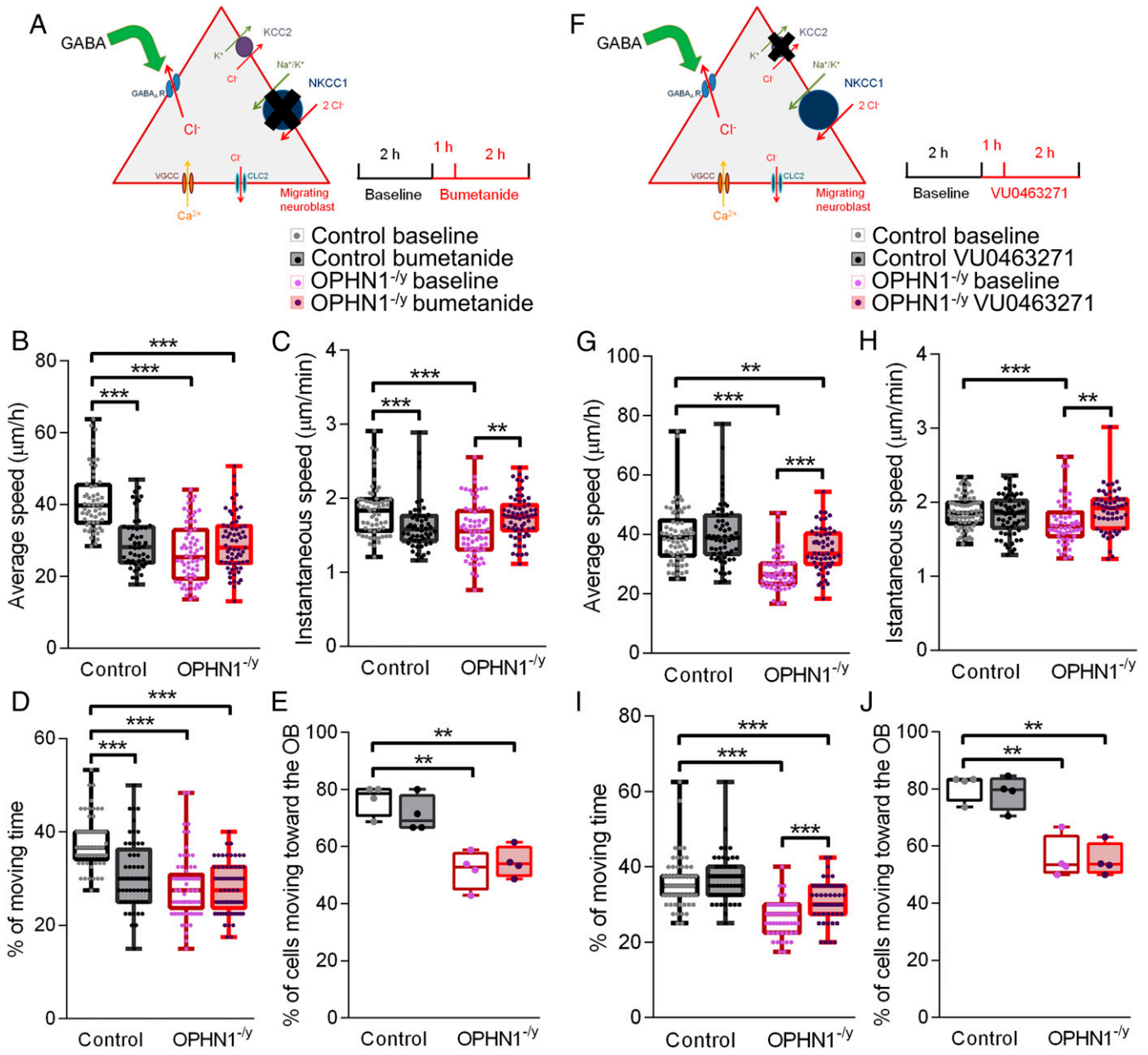

Fig. 6. Blocking the chloride cotransporters has opposite effects on the motility of neuroblasts in controls and OPHN1$^{-/y}$ mice. (*A*) Schematic of an immature neuron that mostly expresses the cotransporter NKCC1 which favors high intracellular Cl^- concentration ($[Cl^-]_i$). The inset shows the scheme of bumetanide, a blocker of NKCC1, delivery in perfusion during time-lapse imaging. (*B–E*) Impact of acute administration of bumetanide on neuroblast migration in controls (black boxes) and in OPHN1$^{-/y}$ mice (red boxes). (*B*) Bumetanide reduces average migration speed in WT mice, with no effect on OPHN1$^{-/y}$ mice. (*C*) Upon bumetanide application, instantaneous speed is reduced in controls while it is increased in mutants. (*D*) Bumetanide decreases the percentage of moving time in WT mice, with no effect on OPHN1$^{-/y}$ mice. (*E*) Directionality of migration is not affected by bumetanide. (*F*) Schematic of a mature neuron that mostly expresses the Cl^- cotransporter KCC2, which leads to low $[Cl^-]_i$. The inset shows the scheme of VU0463271, a blocker of KCC2, delivery in perfusion during time-lapse imaging. (*G–J*) Effects of the blocker of KCC2 on the progression of migrating neuroblasts in controls (black boxes) and in OPHN1$^{-/y}$ mice (red boxes). Acute administration of VU0463271 has no effect on migration in controls; however, it significantly increases (*G*) average migration speed, (*H*) instantaneous speed, and (*I*) percentage of moving time in OPHN1$^{-/y}$ mice. (*J*) Directionality of migration is not affected by VU0463271. Bars = minimum to maximum. *P* values: 0.001 < ** < 0.01; *** < 0.001.

therefore alter the finely regulated actin polymerization, leading to multipolar cells that progress at a lower speed and with no preferential directionality.

Besides being highly conserved regulators of actin cytoskeleton dynamics, Rho GTPases are key signaling intermediates between external stimuli and changes in neuronal morphology and guidance (52, 53). To this end, the tubular structures formed by specialized astrocytes support and isolate migrating cells from the surrounding parenchyma. They also mediate the molecular communication between NPC and extracellular stimuli, exerting a key role in the regulation of GABA and glutamatergic signaling, neurotrophin (i.e., BDNF), and axon guidance molecules (such as Robo and Eprhin) (52, 54–56). The hypertrophic astrocytic processes in OPHN1$^{-/y}$ mice could be due to the aberrant cytoskeleton rearrangement in astrocytes and/or to the altered signaling between neurons and astrocytes, related to the lack of Rho GAP OPHN1 function. Whatever the mechanism, the disorganized tubular structures contributed to the inefficient migration, as reported in

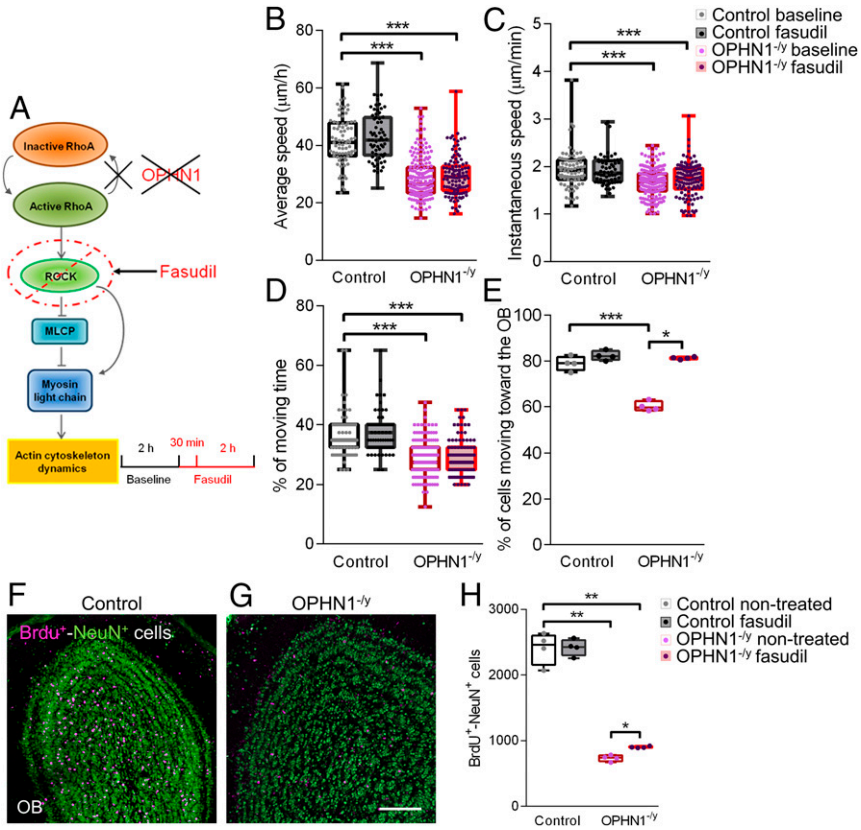

Fig. 7. The ROCK inhibitor fasudil rescues the directionality, without affecting the speed of neuronal precursors in OPHN1$^{-/y}$ mice. (*A–E*) (*A*) Schematic of fasudil target: Fasudil inhibits the ROCK, thus blocking the overactivation of the RhoA/ROCK pathway caused by the loss of function of OPHN1. Bars = minimum to maximum. *P* values: 0.01 < * < 0.05; *** < 0.001. (*B–E*) Effect of acute fasudil administration on the migration of neuroblasts in control mice (black boxes) and OPHN1$^{-/y}$ mice (red boxes). (*B*) Average migration speed. (*C*) Instantaneous speed. (*D*) Percentage of moving time. (*E*) Directionality of migration. Acute fasudil treatment does not affect any of the analyzed parameters of migration in controls; however, in OPHN1$^{-/y}$ mice it completely rescues the directionality of migration of neuronal precursors, without affecting the speed of migration. (*F* and *G*) Representative confocal images of coronal sections of the OB labeled with neuronal nuclei (NeuN, in green) and BrdU (in magenta) in WT mice (*F*) and in OPHN1$^{-/y}$ mice (*G*). (Scale bar: 200 μm.) (*H*) Quantification of newly generated granule cells in the OB at 9 dpi of BrdU upon chronic fasudil treatment in controls and in OPHN1$^{-/y}$ mice. Chronic fasudil treatment did not rescue the complement of adult-born immature interneurons at 9 dpi in the OB of OPHN1$^{-/y}$ mice. Bars = minimum to maximum. *P* values: 0.01 < * < 0.05; 0.001 < ** < 0.01.

several mutant mouse lines in which disruption of the astrocytic tubes is accompanied by impaired migration (54, 57).

Altered Cl$^-$ Homeostasis Hindered the Progression of NPC. We identified alterations in GABA signaling as an additional factor underpinning the phenotype observed in OPHN1$^{-/y}$ mice. We found that GABA application reduced the average speed of neuroblast migration in WT controls but increased the progression speed in OPHN1$^{-/y}$ mice. Similarly, bicuculline triggered opposite effects on the migration speed in WT controls and OPHN1$^{-/y}$ mice. We found that the altered responses to GABA were associated with the premature decrement of $[Cl^-]_i$ in mutant NPC caused by the early overexpression of KCC2. Because of this precocious development of Cl$^-$ homeostasis, the precursors were insensitive to bumetanide, a blocker of NKCC1, but were sensitive to a KCC2 blocker, whose application restored the migration speed. The untimely overexpression of KCC2 in OPHN1$^{-/y}$ NPC switched the responsiveness of neuroblasts to GABA from a motogenic to a stop signal. This has also been observed in inhibitory interneurons precursors en route to the cortex, in which overexpression of KCC2 leads to a premature stop in erratic locations (58). Similar results were observed also in migrating neurons in other mammalian species (59, 60). It is noteworthy that the premature arrest of NPC results in the massive death of dislocated neuroblasts and, consequently, in the dramatic reduction of the number of NPC that reach the OB, as reported in Redolfi et al. (16).

The relative expression of the cotransporters NKCC1 and KCC2 defines the $[Cl^-]_i$ that in turn affects the reversal potential of Cl$^-$ (E_{Cl^-}) and therefore the direction of the current flowing through $GABA_A$Rs (18). Despite its critical role in defining the GABA response, $[Cl^-]_i$ has rarely been measured in vivo. Here, we overcame this limitation by taking advantage of a new genetically encoded $[Cl^-]_i$ sensor (17) specifically designed for deep imaging in vivo and we directly measured $[Cl^-]_i$ in acute thick slices with single-cell resolution. This approach has the invaluable advantage of allowing the direct measurement of $[Cl^-]_i$ in a large population of cells. We found that in WT migrating precursors $[Cl^-]_i$ has a mean larger than 30 mM, a situation that recapitulates the developmental pattern observed in cortical neurons (17). In contrast, $[Cl^-]_i$ was significantly lower in OPHN1$^{-/y}$ migrating cells than in controls, due to the higher expression of KCC2 (discussed above) that suggested an early maturation of the chloride gradient in mutant mice.

As a further demonstration of the striking difference in the development of neuronal precursors between control and OPHN1 mutants, we directly measured E_{Cl^-} by gramicidin-perforated patch-clamp recordings. We found that in OPHN1$^{-/y}$ mice the value of E_{Cl^-} was significantly more negative than in WT mice, and

more negative or very close to the value of V_{rest}, resulting in hyperpolarizing or shunting GABA responses. On the contrary, in controls, the value of E_{Cl^-} was dramatically more positive than V_{rest}, consistent with depolarizing GABA responses, that are typical of immature neurons. Our data confirm that V_{rest} has a large dispersion in these immature cells, both in WT and OPHN1$^{-/y}$ mice (61–63). This variability likely reflects the different status of neuroblasts. It is well known that NPC alternate active migration to pauses. As demonstrated for precursors of inhibitory interneurons en route to the cortex (58), the migration and the pausing phases are associated to distinct ion fluxes through the plasma membrane that in turn regulate V_{rest}. Despite the dispersion of values, the average V_{rest} was similar in OPHN1$^{-/y}$ and control cells, while E_{Cl^-} was significantly different in the two groups of mice, indicating that the difference in GABA responses between WT and OPHN1$^{-/y}$ mice is due to the different $[Cl^-]_i$ and not to V_{rest}.

Altogether, our data provide compelling evidence that the slower progression of OPHN1$^{-/y}$ migrating cells along the RMS is due to the abnormal development of Cl^- homeostasis that affects the response elicited by GABA in migrating cells.

The mechanism underlying the increased level of KCC2 associated with OPHN1 mutation remains elusive. In physiological conditions, KCC2 expression is high in mature neurons (64, 65) and in inhibitory interneurons that have reached their final destination in the cortex (58). Evidence indicates that multiple signaling pathways and several cell/tissue-specific mechanisms underlie KCC2 transcription and translation (66, 67). That being said, it is conceivable that the abnormal actin-cytoskeleton dynamics associated with the loss of function of the Rho GAP OPHN1 in migrating cells leads to altered communication between extracellular cues and intracellular signaling pathways that control gene expression, leading to the increased expression level of KCC2. Among these factors, GABA and BDNF, abundantly present in the RMS, have been involved in the regulation of KCC2 expression, although conflicting results are present in the literature (58, 63–65). Additionally, the hindered progression of mutated NPC could favor KCC2 expression as NPC stationarity might be interpreted by the intracellular signaling as an indication that the target is reached, thus triggering the gene expression profile proper of mature neurons.

OPHN1 Downstream Enhanced RhoA Signaling Impairs Directionality of NPC. We found that the directionality of migrating cells was not affected by the pharmacological treatments that modulate GABA signaling, suggesting that this feature is regulated by different mechanisms. Several studies indicate that ID associated with OPHN1 mutation is in part due to the enhanced ROCK signaling (40, 41), which leads to the deregulation of actin cytoskeleton dynamics (16, 39, 51, 68). Indeed, the pharmacological inhibition of ROCK was reported to rescue some of the defects triggered by OPHN1 mutation (16, 42, 43), including the reduced number of neuronal precursors that reach the OB (16). By time-lapse imaging of migrating cells, here we show that acute treatment with fasudil completely rescued the directionality of OPHN1$^{-/y}$ migrating cells with no effect on migration speed, and this was confirmed by our in vivo data. We found that upon fasudil chronic treatment only a portion of the newly generated cells reached the OB at 9 dpi, while by 15 dpi the entire complement of new cells was present in the bulb in OPHN1$^{-/y}$ mice (16). Altogether these results confirmed that fasudil treatment rescues the directionality but not the speed of NPC.

Migration is a fundamental process that allows neurons to reach their target at a specific time. Our data show that the loss of function of OPHN1 causes an error in migration that is present through the lifetime of the individual, potentially affecting brain computation in all areas that rely on the integration of newborn neurons. Additional studies are required to understand the consequence of a slower progression and delayed integration of new neurons into OB circuitry, and likely into cortical and subcortical areas.

Conclusion

Altogether, our data demonstrate that OPHN1 mutation deeply impairs postnatal forebrain GABAergic migration affecting specific features of cell motility that are regulated by distinct pathways. Namely, we found that overactivation of the RhoA downstream signaling leads to aberrant actin-cytoskeleton rearrangement, which in turn causes abnormal cell morphology, motility, and directionality, as confirmed by the action of fasudil. The speed of migrating neuroblasts appears to be regulated by the driving force of Cl^- through $GABA_A$Rs. The premature increased expression of KCC2 and its consequence on the Cl^- homeostasis, triggered by OPHN1 mutation in neuroblasts, stands out as a novel factor in the current scenario, in which the prevailing expression of NKCC1 in mature cells is considered the culprit of several neurological disorders, such as Down syndrome and Rett syndrome (20). Consistently, the NKCC1 blocker, bumetanide, restoring low $[Cl^-]_i$ was reported to attenuate symptoms and pathology of many disorders in experimental and clinical trials (20–23). Our findings open a different perspective, in which a wider range of $[Cl^-]_i$ shades could be associated with pathological situations, posing the need to characterize the specific alteration of Cl^- homeostasis to design tailored therapeutic approaches. This specificity is likely to be the key to effective treatments. At the same time, our findings unveil the limitation of monotherapeutic approaches, such as fasudil, that can implement a partial rescue since it affects only a single signaling pathway.

Methods

Mutant Line Mice. Animals were housed in filtered cages in a temperature-controlled room, with 12/12-h dark/light cycle with ad libitum access to water and food.

All animal experiments conformed to the European Union Directive 2010/63/EU for animal experiments and to the Animal Research: Reporting of In Vivo Experiments guidelines. Experimental protocols were approved by the Italian Ministry of Health. For details, see *SI Appendix, Supplementary Methods*.

Stereotaxic Injection in the SVZ. Viral vectors were stereotaxically injected in the SVZ (4 μL volume at 1×10^{10} TU/mL, for LV-eGFP, 1.46×10^9, for LV-mKateN2, titer) to label neuronal precursor cells at the following stereotaxic coordinates, relative to Bregma: anterior = 1 mm; lateral = 1 mm; depth = 2.5 mm. For details, see *SI Appendix, Supplementary Methods*.

Postnatal Electroporation in the SVZ. Two microliters of LssClopHensor plasmid (4 μg/μl) was injected with a Hamilton syringe in the lateral ventricle (LV), identified as a site approximately equidistant from the lambdoid suture and the eye, 2 mm lateral to the sagittal suture and 2 mm deep from the scalp surface. For details, see *SI Appendix, Supplementary Methods*.

BrdU Injections. BrdU (50 mg/kg) was injected four times with 2-h intervals. For details, see *SI Appendix, Supplementary Methods*.

Immunohistochemistry. Floating sagittal sections (70 μm thick) or coronal sections (60 μm thick) were incubated overnight at 4 °C with the following primary antibodies: goat immunoglobulin G (IgG) anti-DCX (neuronal precursors marker DCX, 1:1,000; Santa Cruz Biotechnology), rabbit IgG anti-GFAP (1:2,500; Abcam), rat monoclonal anti BrdU (1:200; Abcam) and mouse monoclonal anti NeuN (neuronal marker Neuronal Nuclear antigen, 1:200; Millipore). Primary antibodies were visualized with the following secondary antibodies: Cy3 conjugate anti-goat IgG (1:800; Jackson Laboratories), Alexa Fluor 488 conjugate anti-rabbit IgG (1:800; Jackson Laboratories), Cy3 conjugate anti-rat IgG (1:800; Jackson Laboratories), DyLight 488 conjugate anti-mouse IgG (1:800; Jackson Laboratories), and Alexa Fluor 488 conjugate anti-rat IgG (1:800; Jackson Laboratories). For details, see *SI Appendix, Supplementary Methods*.

Chronic Drug Administration. OPHN1$^{-/y}$ mice and WT littermate controls were treated with the ROCK and PKA kinases noncompetitive inhibitor fasudil, also known as HA1077 (Selleck Chemicals), at postnatal day 30. For details, see *SI Appendix, Supplementary Methods*.

Image Analysis and Quantification. Whole-brain images were taken at the stereomicroscope (Leica MZ16F) equipped with a PLANPO 0.63 objective (Leica), and a camera (Canon Eos 1000D). Sections were analyzed at the confocal microscope (Zeiss LSM 700) equipped with an EC Plan-Neofluar 20×/0.50 M27 objective (Zeiss), or with a Plan-APOCHROMAT 63×/1.4 oil DIC objective (Zeiss). For details, see *SI Appendix, Supplementary Methods*).

Two-Photon Time-Lapse Imaging of Migrating Precursors along the RMS. Time-lapse imaging of GFP-labeled migrating neuroblasts in acute slices was performed using a two-photon microscope (Scientifica 2P, Ti:sapphire-based laser, Cameleon Ultra II; Coherent) equipped with a 16×/0.8 numerical aperture DIC N2 water immersion objective (Olympus). Each Z-stack was 512 × 512 pixels, 100 μm thick, and was acquired at 0.86 frame per second. A Z-stack was acquired every 3 min and 40 total Z-stacks were acquired for each imaging session. This allowed us to follow the migration process along the same field of view for a total time of 2 h for each condition. For details, see *SI Appendix, Supplementary Methods*.

Acute Drug Administration. The drugs GABA (Sigma-Aldrich), bicuculline ($GABA_A$ receptors inhibitor; Sigma-Aldrich), bumetanide (NKCC1 inhibitor; Sigma-Aldrich), VU0463271 (KCC2 inhibitor; Sigma-Aldrich), fasudil (HA1077, ROCK2, and PKA inhibitor; Selleck Chemicals) were suspended in artificial cerebrospinal fluid (ACSF) or dimethyl sulfoxide (DMSO) following the data sheet information and then diluted to the final concentration in oxygenated ACSF at 32 °C and continuously perfused into the imaging chamber. For details, see *SI Appendix, Supplementary Methods*.

Tracking of Migrating Neuroblasts along the RMS. The motility of migrating neuroblasts was tracked and computed with ImageJ software (NIH) by using different parameters: 1) average speed, considering the average translocation speed of precursors in 1 h of time-lapse imaging including both migrating and pausing phases, 2) instantaneous speed that indicates cell migration speed exclusively in the translocation phase, 3) moving time, indicating the amount of time cells spend in the migratory phase, and 4) directionality of migration. For details, see *SI Appendix, Supplementary Methods*.

Chloride Imaging along the RMS. ClopHensor was imaged at four excitation wavelengths: 830 nm, 860 nm, 910 nm, and 960 nm. For details, see *SI Appendix, Supplementary Methods*.

Western Blotting. Membranes were not stripped and probed for the following primary antibodies: mouse anti-mouse NKCC1 (1:1,000, clone T4 DSHB; University of Iowa), rabbit anti-KCC2 (1:1,000; Millipore), and mouse anti-GADPH (1:5,000; Sigma-Aldrich). Secondary antibodies were horseradish peroxidase-conjugated anti-mouse IgG (1:5,000; GE Healthcare) in T-PBS Tween-20 0.05% + 5% nonfat dry milk (Sigma-Aldrich) and horseradish peroxidase-conjugated anti-rabbit IgG (1:5,000; GE Healthcare) in PBS Tween-20 0.05% + 5% nonfat dry milk (Sigma-Aldrich). For details, see *SI Appendix, Supplementary Methods*.

Gramicidin-Perforated Patch-Clamp Recordings. Gramicidin-perforated recordings were performed in voltage clamp configuration using a multiclamp 700B amplifier (Molecular Devices). Signals were filtered at 1 kHz and sampled at 10 kHz with a Digidata 1440 s interface and pClamp 10 software (Molecular Devices). Gramicidin (368020; Merck-Millipore) was added to the intracellular solution at a final concentration of 80 μg/mL from a stock 10 mg/mL in DMSO. Input and access resistance were directly tested in a subset of cells with 5-mV steps, resulting respectively in 1.33 ± 0.31 GOhm and 62.9 ± 4.4 MOhm (n = 5, WT). Currents were evoked by local pressure pulse applications of the selective $GABA_AR$ agonist muscimol (100 μM) contained in patch pipettes located in proximity to the recorded cell, above the tissue. For details, see *SI Appendix, Supplementary Methods*.

Data Availability. All data are included in the paper and in supporting information.

ACKNOWLEDGMENTS. We thank all members of the C.L. laboratory for support and insightful discussion. We thank P. Billuart for generously providing the $OPHN1^{-/y}$ mice. This work was supported by Telethon GGP11116 and GGP19281, Ministero dell'Istruzione, dell'Università e della Ricerca-Consiglio Nazionale delle Ricerche Nanomax (to C.L.).

1. P. Billuart *et al.*, Oligophrenin 1 encodes a rho-GAP protein involved in X-linked mental retardation. *Pathol. Biol. (Paris)* **46**, 678 (1998).
2. F. Fauchereau *et al.*, The RhoGAP activity of OPHN1, a new F-actin-binding protein, is negatively controlled by its amino-terminal domain. *Mol. Cell. Neurosci.* **23**, 574–586 (2003).
3. E. E. Govek *et al.*, The X-linked mental retardation protein oligophrenin-1 is required for dendritic spine morphogenesis. *Nat. Neurosci.* **7**, 364–372 (2004).
4. P. Billuart, J. Chelly, S. Gilgenkrantz, [X-linked mental retardation]. *Med. Sci. (Paris)* **21**, 947–953 (2005).
5. M. Khelfaoui *et al.*, Loss of X-linked mental retardation gene oligophrenin1 in mice impairs spatial memory and leads to ventricular enlargement and dendritic spine immaturity. *J. Neurosci.* **27**, 9439–9450 (2007).
6. N. Nadif Kasri, A. Nakano-Kobayashi, R. Malinow, B. Li, L. Van Aelst, The Rho-linked mental retardation protein oligophrenin-1 controls synapse maturation and plasticity by stabilizing AMPA receptors. *Genes Dev.* **23**, 1289–1302 (2009).
7. N. Gogolla *et al.*, Common circuit defect of excitatory-inhibitory balance in mouse models of autism. *J. Neurodev. Disord.* **1**, 172–181 (2009).
8. O. Marín, Interneuron dysfunction in psychiatric disorders. *Nat. Rev. Neurosci.* **13**, 107–120 (2012).
9. S. Coghlan *et al.*, GABA system dysfunction in autism and related disorders: From synapse to symptoms. *Neurosci. Biobehav. Rev.* **36**, 2044–2055 (2012).
10. D. Inta *et al.*, Neurogenesis and widespread forebrain migration of distinct GABAergic neurons from the postnatal subventricular zone. *Proc. Natl. Acad. Sci. U.S.A.* **105**, 20994–20999 (2008).
11. N. Sanai *et al.*, Unique astrocyte ribbon in adult human brain contains neural stem cells but lacks chain migration. *Nature* **427**, 740–744 (2004).
12. N. Sanai *et al.*, Corridors of migrating neurons in the human brain and their decline during infancy. *Nature* **478**, 382–386 (2011).
13. M. F. Paredes *et al.*, Extensive migration of young neurons into the infant human frontal lobe. *Science* **354**, aaf7073 (2016).
14. P. M. Lledo, M. Alonso, M. S. Grubb, Adult neurogenesis and functional plasticity in neuronal circuits. *Nat. Rev. Neurosci.* **7**, 179–193 (2006).
15. F. Lazarini, P. M. Lledo, Is adult neurogenesis essential for olfaction? *Trends Neurosci.* **34**, 20–30 (2011).
16. N. Redolfi *et al.*, Oligophrenin-1 regulates number, morphology and synaptic properties of adult-born inhibitory interneurons in the olfactory bulb. *Hum. Mol. Genet.* **25**, 5198–5211 (2016).
17. S. Sulis Sato *et al.*, Simultaneous two-photon imaging of intracellular chloride concentration and pH in mouse pyramidal neurons in vivo. *Proc. Natl. Acad. Sci. U.S.A.* **114**, E8770–E8779 (2017).
18. Y. Ben-Ari, Excitatory actions of gaba during development: The nature of the nurture. *Nat. Rev. Neurosci.* **3**, 728–739 (2002).
19. K. Kaila, E. Ruusuvuori, P. Seja, J. Voipio, M. Puskarjov, GABA actions and ionic plasticity in epilepsy. *Curr. Opin. Neurobiol.* **26**, 34–41 (2014).
20. Y. Ben-Ari, NKCC1 chloride importer antagonists attenuate many neurological and psychiatric disorders. *Trends Neurosci.* **40**, 536–554 (2017).
21. E. Lemonnier *et al.*, Effects of bumetanide on neurobehavioral function in children and adolescents with autism spectrum disorders. *Transl. Psychiatry* **7**, e1124 (2017).
22. A. E. Hernan, G. L. Holmes, Antiepileptic drug treatment strategies in neonatal epilepsy. *Prog. Brain Res.* **226**, 179–193 (2016).
23. G. Deidda *et al.*, Early depolarizing GABA controls critical-period plasticity in the rat visual cortex. *Nat. Neurosci.* **18**, 87–96 (2015).
24. C. Lois, J. M. García-Verdugo, A. Alvarez-Buylla, Chain migration of neuronal precursors. *Science* **271**, 978–981 (1996).
25. F. Doetsch, I. Caillé, D. A. Lim, J. M. García-Verdugo, A. Alvarez-Buylla, Subventricular zone astrocytes are neural stem cells in the adult mammalian brain. *Cell* **97**, 703–716 (1999).
26. D. A. Lim, A. Alvarez-Buylla, The adult ventricular-subventricular zone (V-SVZ) and olfactory bulb (OB) neurogenesis. *Cold Spring Harb. Perspect. Biol.* **8**, a018820 (2016).
27. F. J. Martini *et al.*, Biased selection of leading process branches mediates chemotaxis during tangential neuronal migration. *Development* **136**, 41–50 (2009).
28. N. Kaneko, M. Sawada, K. Sawamoto, Mechanisms of neuronal migration in the adult brain. *J. Neurochem.* **141**, 835–847 (2017).
29. R. Shinohara *et al.*, A role for mDia, a Rho-regulated actin nucleator, in tangential migration of interneuron precursors. *Nat. Neurosci.* **15**, 373–380 (2012).
30. B. T. Schaar, S. K. McConnell, Cytoskeletal coordination during neuronal migration. *Proc. Natl. Acad. Sci. U.S.A.* **102**, 13652–13657 (2005).
31. J. W. Tsai, K. H. Bremner, R. B. Vallee, Dual subcellular roles for LIS1 and dynein in radial neuronal migration in live brain tissue. *Nat. Neurosci.* **10**, 970–979 (2007).
32. A. J. Bolteus, A. Bordey, GABA release and uptake regulate neuronal precursor migration in the postnatal subventricular zone. *J. Neurosci.* **24**, 7623–7631 (2004).
33. S. Mejia-Gervacio, K. Murray, P. M. Lledo, NKCC1 controls GABAergic signaling and neuroblast migration in the postnatal forebrain. *Neural Dev.* **6**, 4 (2011).
34. V. C. Cuzon, P. W. Yeh, Q. Cheng, H. H. Yeh, Ambient GABA promotes cortical entry of tangentially migrating cells derived from the medial ganglionic eminence. *Cereb. Cortex* **16**, 1377–1388 (2006).
35. J. A. Bagley, L. Belluscio, Dynamic imaging reveals that brain-derived neurotrophic factor can independently regulate motility and direction of neuroblasts within the rostral migratory stream. *Neuroscience* **169**, 1449–1461 (2010).
36. D. D. Wang, D. D. Krueger, A. Bordey, GABA depolarizes neuronal progenitors of the postnatal subventricular zone via GABAA receptor activation. *J. Physiol.* **550**, 785–800 (2003).
37. L. Nguyen *et al.*, Autocrine/paracrine activation of the GABA(A) receptor inhibits the proliferation of neurogenic polysialylated neural cell adhesion molecule-positive

(PSA-NCAM+) precursor cells from postnatal striatum. *J. Neurosci.* **23**, 3278–3294 (2003).
38. K. Kaila, T. J. Price, J. A. Payne, M. Puskarjov, J. Voipio, Cation-chloride cotransporters in neuronal development, plasticity and disease. *Nat. Rev. Neurosci.* **15**, 637–654 (2014).
39. M. Khelfaoui *et al*., Inhibition of RhoA pathway rescues the endocytosis defects in Oligophrenin1 mouse model of mental retardation. *Hum. Mol. Genet.* **18**, 2575–2583 (2009).
40. G. J. Ramakers, Rho proteins, mental retardation and the cellular basis of cognition. *Trends Neurosci.* **25**, 191–199 (2002).
41. K. Riento, A. J. Ridley, Rocks: Multifunctional kinases in cell behaviour. *Nat. Rev. Mol. Cell Biol.* **4**, 446–456 (2003).
42. M. Khelfaoui *et al*., Lack of the presynaptic RhoGAP protein oligophrenin1 leads to cognitive disabilities through dysregulation of the cAMP/PKA signalling pathway. *Philos. Trans. R. Soc. Lond. B Biol. Sci.* **369**, 20130160 (2013).
43. H. Meziane *et al*., Fasudil treatment in adult reverses behavioural changes and brain ventricular enlargement in Oligophrenin-1 mouse model of intellectual disability. *Hum. Mol. Genet.* **25**, 2314–2323 (2016).
44. L. Petreanu, A. Alvarez-Buylla, Maturation and death of adult-born olfactory bulb granule neurons: Role of olfaction. *J. Neurosci.* **22**, 6106–6113 (2002).
45. L. Luo, Rho GTPases in neuronal morphogenesis. *Nat. Rev. Neurosci.* **1**, 173–180 (2000).
46. A. Hall, G. Lalli, Rho and Ras GTPases in axon growth, guidance, and branching. *Cold Spring Harb. Perspect. Biol.* **2**, a001818 (2010).
47. D. Spiering, L. Hodgson, Dynamics of the Rho-family small GTPases in actin regulation and motility. *Cell Adhes. Migr.* **5**, 170–180 (2011).
48. T. Hikita, A. Ohno, M. Sawada, H. Ota, K. Sawamoto, Rac1-mediated indentation of resting neurons promotes the chain migration of new neurons in the rostral migratory stream of post-natal mouse brain. *J. Neurochem.* **128**, 790–797 (2014).
49. K. Khodosevich, P. H. Seeburg, H. Monyer, Major signaling pathways in migrating neuroblasts. *Front. Mol. Neurosci.* **2**, 7 (2009).
50. H. Ota *et al*., Speed control for neuronal migration in the postnatal brain by Gmip-mediated local inactivation of RhoA. *Nat. Commun.* **5**, 4532 (2014).
51. E. E. Govek, S. E. Newey, L. Van Aelst, The role of the Rho GTPases in neuronal development. *Genes Dev.* **19**, 1–49 (2005).
52. H. A. Mason, S. Ito, G. Corfas, Extracellular signals that regulate the tangential migration of olfactory bulb neuronal precursors: Inducers, inhibitors, and repellents. *J. Neurosci.* **21**, 7654–7663 (2001).
53. C. H. Coles, E. Y. Jones, A. R. Aricescu, Extracellular regulation of type IIa receptor protein tyrosine phosphatases: Mechanistic insights from structural analyses. *Semin. Cell Dev. Biol.* **37**, 98–107 (2015).
54. N. Kaneko *et al*., New neurons clear the path of astrocytic processes for their rapid migration in the adult brain. *Neuron* **67**, 213–223 (2010).
55. J. C. Conover *et al*., Disruption of Eph/ephrin signaling affects migration and proliferation in the adult subventricular zone. *Nat. Neurosci.* **3**, 1091–1097 (2000).
56. J. C. Platel *et al*., NMDA receptors activated by subventricular zone astrocytic glutamate are critical for neuroblast survival prior to entering a synaptic network. *Neuron* **65**, 859–872 (2010).
57. R. Belvindrah, S. Hankel, J. Walker, B. L. Patton, U. Müller, Beta1 integrins control the formation of cell chains in the adult rostral migratory stream. *J. Neurosci.* **27**, 2704–2717 (2007).
58. D. Bortone, F. Polleux, KCC2 expression promotes the termination of cortical interneuron migration in a voltage-sensitive calcium-dependent manner. *Neuron* **62**, 53–71 (2009).
59. F. T. Djankpa, F. Lischka, M. Chatterjee, S. L. Juliano, KCC2 manipulation alters features of migrating interneurons in ferret neocortex. *Cereb. Cortex* **29**, 5072–5084 (2019).
60. M. Yeo *et al*., Bisphenol A delays the perinatal chloride shift in cortical neurons by epigenetic effects on the Kcc2 promoter. *Proc. Natl. Acad. Sci. U.S.A.* **110**, 4315–4320 (2013).
61. D. D. Wang, D. D. Krueger, A. Bordey, Biophysical properties and ionic signature of neuronal progenitors of the postnatal subventricular zone in situ. *J. Neurophysiol.* **90**, 2291–2302 (2003).
62. A. Carleton, L. T. Petreanu, R. Lansford, A. Alvarez-Buylla, P. M. Lledo, Becoming a new neuron in the adult olfactory bulb. *Nat. Neurosci.* **6**, 507–518 (2003).
63. D. P. Darcy, J. S. Isaacson, L-type calcium channels govern calcium signaling in migrating newborn neurons in the postnatal olfactory bulb. *J. Neurosci.* **29**, 2510–2518 (2009).
64. D. Arosio, G. M. Ratto, Twenty years of fluorescence imaging of intracellular chloride. *Front. Cell. Neurosci.* **8**, 258 (2014).
65. L. Cancedda, H. Fiumelli, K. Chen, M. M. Poo, Excitatory GABA action is essential for morphological maturation of cortical neurons in vivo. *J. Neurosci.* **27**, 5224–5235 (2007).
66. K. Ganguly, A. F. Schinder, S. T. Wong, M. Poo, GABA itself promotes the developmental switch of neuronal GABAergic responses from excitation to inhibition. *Cell* **105**, 521–532 (2001).
67. C. Rivera, J. Voipio, K. Kaila, Two developmental switches in GABAergic signalling: The K+-Cl- cotransporter KCC2 and carbonic anhydrase CAVII. *J. Physiol.* **562**, 27–36 (2005).
68. C. Gonzalez-Billault *et al*., The role of small GTPases in neuronal morphogenesis and polarity. *Cytoskeleton (Hoboken)* **69**, 464–485 (2012).